

Rapid ice shelf rift propagation

Bradley Paul Lipovsky

¹Department of Earth and Planetary Sciences, Harvard University

Key Points:

- I infer ice shelf wave-induced stresses and then relate these stresses to a rift propagation criterion based in inertial fracture mechanics.
- The lack of rift propagation during periods of high wave-induced stresses suggests the existence of rift cohesive strengthening.
- Ice shelf rifts may be stabilized as they propagate into deeper water or thinner ice.

Abstract

Distant storms, tsunamis, and earthquakes generate waves on floating ice shelves. Previous studies, however, have disagreed about whether the resulting wave-induced stresses may cause ice shelf rift propagation. Most ice shelf rifts show long periods of dormancy suggesting that they have low background stress concentrations and may therefore be susceptible to wave-induced stresses. Here, I quantify wave-induced stresses on the Ross Ice Shelf Nascent Rift and the Amery Ice Shelf Loose Tooth T2 Rift using passive seismology. I then relate these stresses to a fracture mechanical model of rift propagation that accounts for rift cohesive strength due to refrozen melange, ice inertia, and spatial heterogeneity in fracture toughness due to the presence of high toughness suture zones. I infer wave-induced stresses using the wave impedance tensor, a rank three tensor that relates seismically observable particle velocities to components of the stress tensor. I find that wave-induced stresses are an order of magnitude larger on the Ross Ice Shelf as compared to the Amery Ice Shelf. In the absence of additional rift strength, my model predicts that the Nascent Rift should have experienced extensive rift propagation. The observation that no such propagation occurred during this time therefore suggests that the Nascent Rift experiences cohesive strengthening from either refrozen melange or rift tip processes zone dynamics. This study illustrates one way in which passive seismology may illuminate glacier calving physics.

1 Introduction

Floating ice shelves exert a net buttressing force on grounded ice and therefore support the stability of ice sheets [Doake *et al.*, 1998; Rignot *et al.*, 2004; Scambos *et al.*, 2004]. The extent of ice shelves is often limited by the formation of 10 to 100 km long, through-thickness fractures called rifts. Rifts tend to grow in length until they connect to the ice front and create a tabular iceberg [Robin, 1979; Shabtaie and Bentley, 1982; Jacobs *et al.*, 1986; Keys *et al.*, 1998]. Observations show that rifts experience most of their growth during episodic bursts of activity [Joughin and MacAyeal, 2005] that last from seconds [Powell, 2015; Banwell *et al.*, 2017] to hours [Bassis *et al.*, 2005]. These short time scales suggest that rift propagation is a brittle process, meaning that during episodes of rift propagation the ice shelf is well-approximated as an elastic solid everywhere except in a small region near the rift tip [Broek, 2012]. Ductile fracture, in contrast, may occur by the slow coalescence of microcracks [Rice and Tracey, 1969; Lemaitre, 1985; Weiss, 2004; Pralong and Funk, 2005; Borstad *et al.*, 2012, 2013; Duddu and Waisman, 2013; Duddu *et al.*, 2013] and results in an essentially viscous-plastic ice rheology. Field observations show that ductile fracture also occurs in ice shelf rifts, although it typically is associated with slower growth [Bassis *et al.*, 2007]. Linear elastic fracture mechanics is well suited to describe brittle fracture and has previously been used in the study of ice shelf rift propagation, crevasse growth, calving, and hydrofracture [Weertman, 1971, 1973; Smith, 1976; Nemat-Nasser *et al.*, 1979; Van der Veen, 1998; Rist *et al.*, 2002; Larour *et al.*, 2004a; Alley *et al.*, 2005; Krawczynski *et al.*, 2009; Scambos *et al.*, 2009a; Plate *et al.*, 2012; Krug *et al.*, 2014; Yu *et al.*, 2017].

Brittle fracture is driven by loading applied to sharp geometrical features such as the tip of an ice shelf rift [Griffith, 1921]. The resulting stress concentration may be quantified using the stress intensity factor K [Irwin, 1957]. The stress intensity factor K may in turn be expressed entirely in terms of the loading exerted on a system [Rice, 1968], which in ice shelves consists of contributions from gravity, buoyancy, and interaction with grounded and floating ice [Weertman, 1957; Reeh, 1968]. Catalogs of Antarctic ice shelf rifts, however, show that this loading often results in zero measurable propagation over years to decades of observation [Walker *et al.*, 2013, 2015]. Rift propagation, when it does occur, is typically observed to be highly episodic in time [Bassis *et al.*, 2005]. In the context of linear elastic fracture mechanics, this observation suggests that ice shelf rifts commonly attain a state of stress such that $K < K_c$ and no propagation occurs. I argue that

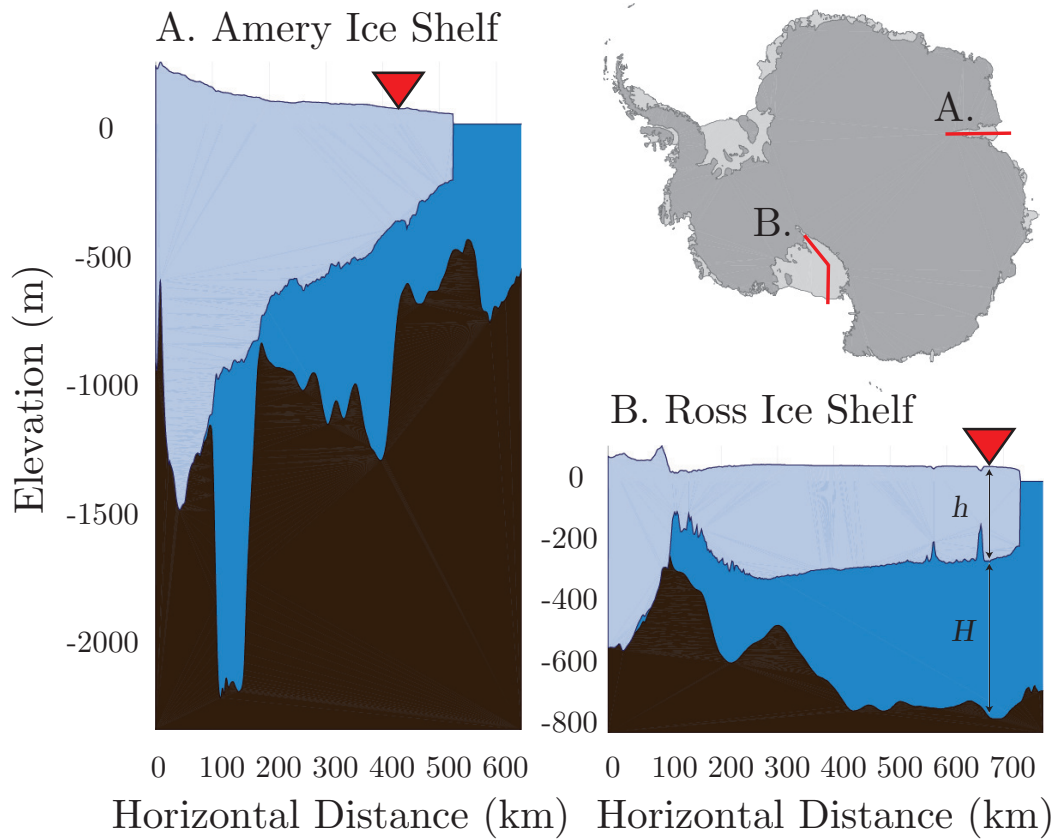
62 this is the precise setting that allows ocean waves to effectively drive episodic ice shelf rift
63 propagation.

64 The exact mechanism responsible for the episodic nature of ice shelf rift propagation
65 remains the subject of multiple competing hypotheses in the literature. Three processes
66 have been proposed as being of importance: spatial heterogeneity of fracture toughness,
67 constitutive instability, and temporal variation in loading due to interaction with ocean
68 waves. In regards to spatial heterogeneity, ice shelf suture zones that form at provenance
69 boundaries in the ice shelf appear to be particularly important. Rapid rift tip propagation
70 events are often observed to terminate when the rift tip reaches an ice shelf suture zone
71 [Hulbe *et al.*, 2010; McGrath *et al.*, 2014; Borstad *et al.*, 2017]. Wave action also appears
72 to play a role. In studies of the Nascent Rift, MacAyeal *et al.* [2006] and Cathles *et al.*
73 [2009] revived the idea of Holdsworth and Glynn [1978] that wave-induced stresses might
74 cause rift propagation. However, Bassis *et al.* [2005, 2007, 2008] also analyzed *in situ*
75 seismic data from the Loose Tooth and concluded that rift propagation there was driven
76 primarily by glacial stresses. Although other studies have appeared to confirm the impor-
77 tance of wave action in rift propagation, these studies were limited by not having *in situ*
78 seismic data. Using remotely sensed imagery, Brunt *et al.* [2011] observed rift propaga-
79 tion following the arrival of a tsunami. Banwell *et al.* [2017] used a nearby seismometer
80 located on bedrock to show that a rift propagation event on the McMurdo Ice Shelf oc-
81 curred during the arrival of large amplitude ocean waves from a distant storm. Finally, a
82 constitutive instability, essentially the opening-mode equivalent of the shearing-mode stick-
83 slip instability [Lipovsky and Dunham, 2016, 2017], has been proposed to be important for
84 episodic rift motion [Larour *et al.*, 2004a]. One of the goals of this paper is to develop a
85 theoretical framework within which to compare the predictions of these hypotheses.

86 Seismometers located directly on floating ice shelves quantify the ice shelf wave
87 field. Using an appropriately defined transfer function called the wave impedance it is
88 therefore possible to calculate stresses from *in situ* velocity seismograms. In a similar
89 vein, Williams and Robinson [1981] used a transfer function approach to estimate water
90 pressure fluctuations from 1 min period gravimeter measurements on the Ross Ice Shelf.
91 The stresses carried by waves in ice shelves have been previously analyzed in an idealized
92 geometry by Holdsworth and Glynn [1978] and Sergienko [2010, 2013] and in more realis-
93 tic geometries by Konovalov [2014] and Sergienko [2017]. Each of these studies, however,
94 calculated the ice shelf response to idealized, monochromatic wave forcing. Here, I build
95 on these previous studies by estimating the stresses associated with the *in situ* ice shelf
96 wave fields as recorded by seismometers located on floating ice shelves. I begin this paper
97 in the first section by describing several observations, including the available seismic data
98 (Section 2). I then derive expressions for the wave impedance in Section 3.

99 I describe a fracture mechanical model of ice shelf rift propagation in Section 4. I
100 then apply this model to the wave-induced stresses inferred at sites near the Ross Ice Shelf
101 Nascent Rift and the Amery Ice Shelf Loose Tooth Rift (Section 5). The principal finding
102 of this analysis is that, in the absence of some additional source of rift cohesive strength,
103 wave-induced stresses are predicted to have been sufficiently large to cause rift propaga-
104 tion on the Nascent Rift. Satellite imagery, however, shows that no observable rift propa-
105 gation occurred during the observation periods under consideration. This finding therefore
106 suggests that the Nascent Rift experienced cohesive strengthening that prevented rift propa-
107 gation during this time. One potential source of this cohesive strength is refreezing in
108 the rift-filling melange [MacAyeal *et al.*, 1998; Rignot and MacAyeal, 1998; Larour *et al.*,
109 2004b; Fricker *et al.*, 2005]. This and other topics are discussed in Section 6.

110 The analysis presented here connects qualitative predictions of ice shelf instability
111 [Holdsworth and Glynn, 1978] to geophysical measurement [MacAyeal *et al.*, 2006; Bassis
112 *et al.*, 2007; Cathles *et al.*, 2009; Brunt *et al.*, 2011; Bromirski *et al.*, 2017] and therefore
113 unleashes the power of seismology to elucidate the detailed mechanics of ice shelf rift
114 propagation.



115 **Figure 1.** Profiles showing the geometry of the Amery (A.) and Ross (B.) Ice Shelves and their position
 116 within the Antarctic Ice Sheet. The red triangles mark the locations of the two seismometers used in this
 117 study. The two cross sections are drawn at the same scale to emphasize geometrical differences between the
 118 two ice shelves.

2 Observations of the Loose Tooth and Nascent Rifts

2.1 Rift propagation behavior

In this paper I analyze two rifts, the Nascent Iceberg Rift on the Ross Ice Shelf and the Loose Tooth T2 Rift on the Amery Ice Shelf. I focus on observation periods during which seismic data is available: November 2005 to May 2006 on the Ross Ice Shelf and January to February 2007 on the Amery Ice Shelf. During these times, the Loose Tooth and Nascent Rifts were 17 and 46 km long [Scambos *et al.*, 2007]. The tip of the Nascent Rift was located in ice with thickness $h = 265$ m. The ocean floor was 691 m below sea level and the sub shelf cavity was therefore $H = 479$ m thick. The tip of the Loose Tooth Rift was located in ice with thickness $h = 301$ m. The ocean floor was 734 m below sea level and the sub shelf cavity was therefore $H = 466$ m thick. These geometries are compared in Figure 1.

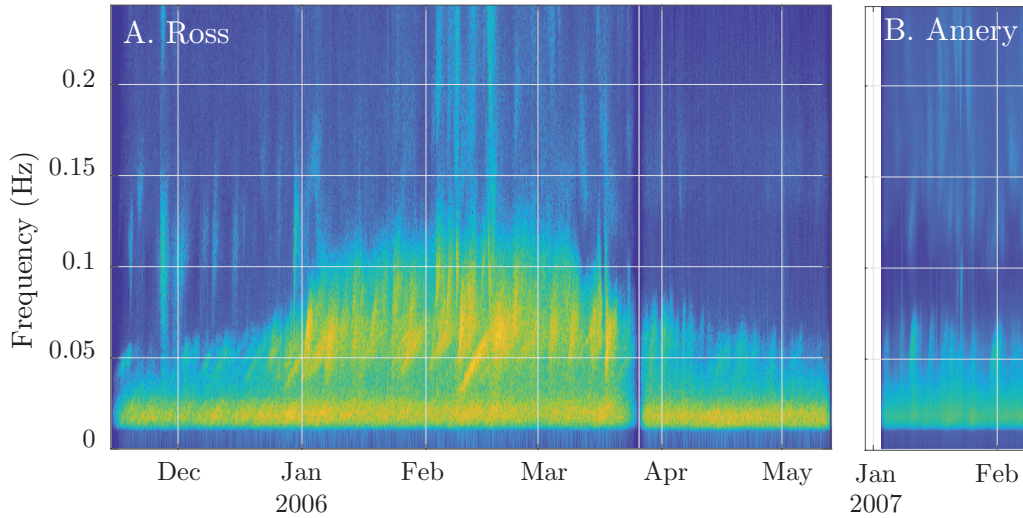
During these time periods, neither rift exhibited measurable rift propagation. This is probably due to the fact that both rifts have propagated into ice suture zones that apparently have higher fracture toughness than the surrounding ice shelf [Borstad *et al.*, 2017]. I reach these conclusions by examining satellite imagery as archived in the Antarctic Ice Shelf Image Archive at the National Snow and Ice Data Center [Scambos *et al.*, 2009b]. These images are captured using the Moderate Resolution Imaging Spectroradiometer (MODIS) instrument. The observation that the Amery did not exhibit propagation during this time has been previously noted by Walker *et al.* [2015]. The nominal resolution of 250 m places an upper bound on the amount of propagation that could go undetected, although because of uncertainties in image analysis Walker *et al.* [2015] uses a great uncertainty of 1 km, which I adopt here.

2.2 Seismic data

I analyze continuously recorded seismograms from seismometers on the Ross and Amery Ice Shelves, Antarctica. These data sets were previously described by MacAyeal *et al.* [2006] and Cathles *et al.* [2009] and by Bassis *et al.* [2008], respectively. I obtain all seismograms from the Incorporated Research Institutions for Seismology (IRIS) Data Management Center website. The locations of the seismometers used in this study are shown in Figure 1.

On the Ross Ice Shelf I examine data from the station RIS2, temporary network code XV, during the 2005-2006 deployment [MacAyeal *et al.*, 2006]. RIS2 was located several km from the tip of the Nascent Rift. From this deployment there are 167 d of data with one outage of several days in late March 2006. On the Amery Ice Shelf I examine data from the station BFN1, temporary network code X9, during a deployment in January 2007. From this deployment there are 36 d of data. Although many other instruments were deployed over a period of several years, I focus on this station because it uses a Guralp CMG-40T seismometer while most other stations use Mark Products L28 seismometers. The CMG-40T has a flat instrumental response down to 0.03 Hz and is therefore expected to be better suited for measuring ocean waves with typical periods of several seconds.

Inferring stresses from seismograms requires interpreting the amplitude information contained in seismic traces. The issue of instrumental response therefore requires special attention. Seismometers have reduced sensitivity to motions below the instrumental sensitivity frequency. When the instrument response is deconvolved from a discretized voltage trace (with units of counts), this insensitivity results in division by a small number, thereby amplifying small amounts of noise. Although geophysically interesting information may be contained at frequencies lower than the instrumental sensitivity frequency, in this study I take a conservative approach and only interpret features in seismograms that occur at frequencies above the sensitivity frequency. I first taper and then bandpass fil-



178 **Figure 2.** Spectrogram of the data from the Ross (A.) and Amery (B.) Ice Shelves. Upward sloping spectral
 179 bands show the arrival of ocean swell from distant storms [Cathles *et al.*, 2009]. Both datasets are plotted
 180 with the same log-power color scale.

169 ter all raw seismic traces. The bandpass filter has cutoff frequencies 0.01, 0.02, 0.2, and
 170 0.4 Hz. I then remove the instrumental response from all seismograms. In all of my anal-
 171 ysis I focus on the LH channels that are sampled at 1 Hz.

172 Spectrograms of the waveforms used in this study shown in the spectrogram in Fig-
 173 ure 2. The principal feature is the arrival of ocean swell from distant storms. These storm
 174 waves appear as upward sloping spectral lines. This occurs because long period ocean
 175 swell travels faster and therefore arrives before short period swell [Munk *et al.*, 1963].
 176 This signal has been described extensively by Cathles *et al.* [2009] and the interested reader
 177 is referred there for more details.

181 3 Wave stresses

182 Seismometers located directly on floating ice shelves measure the Lagrangian par-
 183 ticle velocity, within a certain frequency range, of the parcel of ice on which they rest.
 184 In this section, I derive a transfer function called the wave impedance that relates these
 185 particle velocity perturbations to their associated stresses perturbations. I calculate wave
 186 impedances for two types of long period ice shelf waves: flexural waves and extensional
 187 waves. I will show that there are two main differences between these wave types. First,
 188 the flexural wave impedance is frequency-dependent but the extensional wave impedance
 189 is not. Second, flexural wave impedances tend to be much higher than extensional wave
 190 impedances. These results are summarized in Figures 3 and 4.

191 In order to write down expressions for the wave impedances, it is first necessary
 192 to describe the waves themselves. In Appendix A, I describe ice shelf wave motion in a
 193 finite-thickness elastic ice shelf over an inviscid, incompressible, finite-thickness water
 194 layer and rigid ocean floor. I consider waves that propagate in the direction of flow, and
 195 I treat a two dimensional cross section in the vertical and flow directions. Several limita-
 196 tions associated with these assumptions are discussed in Section 6. In Appendix B I show
 197 that waves with wavelength greater than the ice thickness may propagate as either flexur-
 198 al or extensional waves. I begin this section by describing the general wave impedance
 199 transfer function (Section 3.1).

Shear modulus	μ	3.5 GPa
Young's modulus	E	9.3 GPa
Poisson ratio	ν	0.33
Density of ice	ρ	916 kg/m ³
Density of seawater	ρ_w	1024 kg/m ³
Dilatational wave speed	c_p	3750 m/s
Shear wave speed	c_s	1950 m/s
Fracture toughness	K_C	100 to 400 kPa√m

219

Table 1. Table of ice mechanical properties [Schulson *et al.*, 2009].

200

3.1 Ice shelf wave impedances

201

The transfer function between the perturbation velocity vector component $v_l \equiv \partial u_l / \partial t$ and the perturbation stress tensor component σ_{ij} is called the wave impedance. It is defined as

202

$$Z_{ijl}(k, \omega) = \frac{\Sigma_{ij}(k, \omega)}{(-i\omega)U_l(k, \omega)}. \quad (1)$$

203

204

Here, the subscripts i , j , and l may vary over the three spatial coordinates x , y , and z . The spatial coordinates are defined so that x is in the direction of ice flow, z is positive upwards, and y is perpendicular to x and z following the right-hand-rule. Upper case letters denote the double Fourier transform in time t and in the horizontal direction x . For an arbitrary, adequately smooth function f , the Fourier transform of f is denoted,

205

206

207

208

$$F(k, z, \omega) = \int_{-\infty}^{\infty} \int_{-\infty}^{\infty} f(x, z, t) e^{i(kx - \omega t)} dx dt \quad (2)$$

209

This definition introduces the horizontal wavenumber k and frequency ω .

210

211

The impedance tensor defined in this way allows the estimation of wave field stresses using multiplication in the Fourier domain,

$$\sigma_{ij}(x, t) = \int_{-\infty}^{\infty} \int_{-\infty}^{\infty} Z_{ijl}(k, \omega) U_l(k, \omega) e^{i(kx - \omega t)} dk d\omega. \quad (3)$$

212

213

214

215

The exact form of the wave impedance tensor components depends on the type of wave being considered. For both flexural and extensional waves, the wave impedance is a function of the wave phase velocity. These wave phase velocities are derived in Appendix B, and the associated particle motions are described in Appendix C.

220

3.2 Flexural waves

221

222

223

The impedance of a wave generally depends on the wave phase velocity $c \equiv \omega/k$. Writing in terms of the wavelength $\lambda \equiv 2\pi/k$, the phase velocity of flexural-gravity waves is determined by the dispersion relation

$$\omega^2 = \frac{2\pi g}{\lambda} \frac{(\lambda_{fg}/\lambda)^4 + 1}{2\pi(\rho/\rho_w)h/\lambda + \coth(2\pi H/\lambda)}, \quad (4)$$

224

225

with water layer thickness H , ice thickness h , acceleration due to gravity g , flexural-gravity wave length λ_{fg} ,

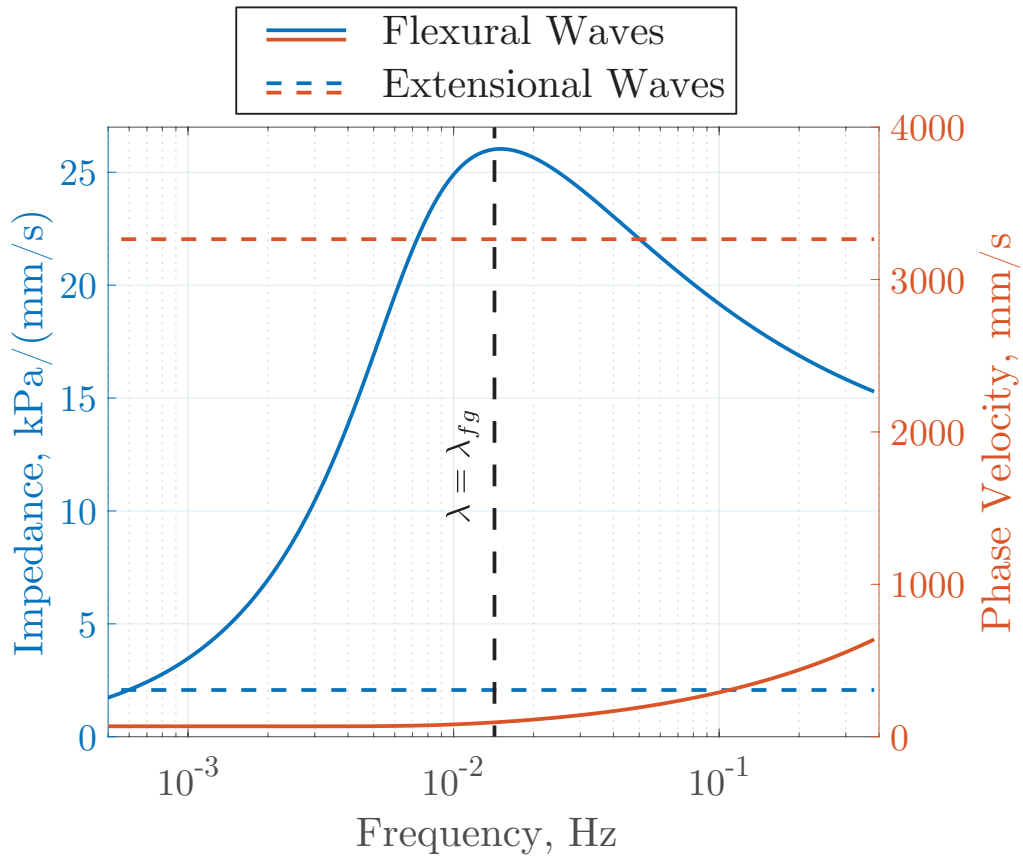
$$\lambda_{fg} \equiv 2\pi \left(\frac{D}{g\rho_w} \right)^{1/4}, \quad (5)$$

226

227

228

flexural rigidity $D \equiv E'h^3$, $E' \equiv E/(1 - \nu^2)$, Young's Modulus E , and Poisson ratio ν . The material properties of ice are listed in Table 1. At the tip of the Nascent and Loose Tooth Riffs, $\lambda_{fg} = 7.1$ km and 7.8 km, respectively [Fretwell *et al.*, 2013].



216 **Figure 3.** Wave speeds and impedances for extensional waves (dashed lines) flexural-gravity waves (solid
 217 lines). For the flexural-gravity waves, the curves are calculated for sub shelf cavity thickness $H = 466$ m and
 218 ice thickness $h = 265$ m. All curves are drawn until $hk = 1/2$, reflecting the long wavelength approximation.

229 The flexural-gravity wave length λ_{fg} separates two regimes of wave behavior (Fig-
 230 ure 3). When $\lambda \gg \lambda_{fg}$ the dispersion relation is identical to that for surface gravity
 231 waves. In contrast, when $\lambda \ll \lambda_{fg}$, the dominant restoring force is elasticity and gravity
 232 does not enter the dispersion relation. As described in detail in Appendix B, this disper-
 233 sion relation is valid for waves with wavelength greater than the ice thickness.

I calculate the flexural mode σ_{xx} -to- u_z impedance component as

$$Z_{xxz}^F = \frac{\Sigma_{xx}}{(-i\omega)U_z} \approx (-i\omega) \frac{hE'}{[c(\omega)]^2}. \quad (6)$$

234 In writing Equation 6, I have used the expressions for the extensional wave stress Σ_{xx} and
 235 vertical displacement U_z derived in Appendix C. The approximate equality symbol reflects
 236 the long wavelength approximation as discussed in Appendix B.

237 This impedance component is plotted in Figure 3. Flexural wave impedance reaches
 238 a maximum at the frequency associated with the flexural-gravity wavelength λ_{fg} . Below
 239 this frequency, impedance increases proportional to frequency ω . Above this frequency,
 240 impedance is a decreasing function of frequency.

241 Flexural stresses, denoted σ_f , may be calculated from a vertical component velocity
 242 seismogram $v_z(t) = \partial u_z / \partial t$ by convolving a velocity time series with the transfer function
 243 in Equation 6,

$$\sigma_f(t) \equiv \sigma_{xx}(t) = E'h \int \frac{(-i\omega)V_z(\omega)}{[c(\omega)]^2} e^{i\omega t} d\omega. \quad (7)$$

244 In this expression I have used the definition of the phase velocity to eliminate reference to
 245 the wavenumber k .

246 A simplified case occurs for wavelengths longer than the water depth H and the
 247 flexural-buoyancy wavelength λ_{fg} . In this case $c^2 = gH$ is nondispersive and therefore
 248 independent of frequency. The integral in Equation 7 may therefore be evaluated as

$$\sigma_f(t) = \frac{E'h}{gH} \frac{\partial V}{\partial t}. \quad (8)$$

249 This result is interesting because it shows that waves in the gravity limit have stresses that
 250 are proportional to particle acceleration. This is in contrast to body waves which have
 251 stresses that are proportional to particle velocity.

258 3.3 Extensional waves

259 Extensional waves have nondispersive phase velocity

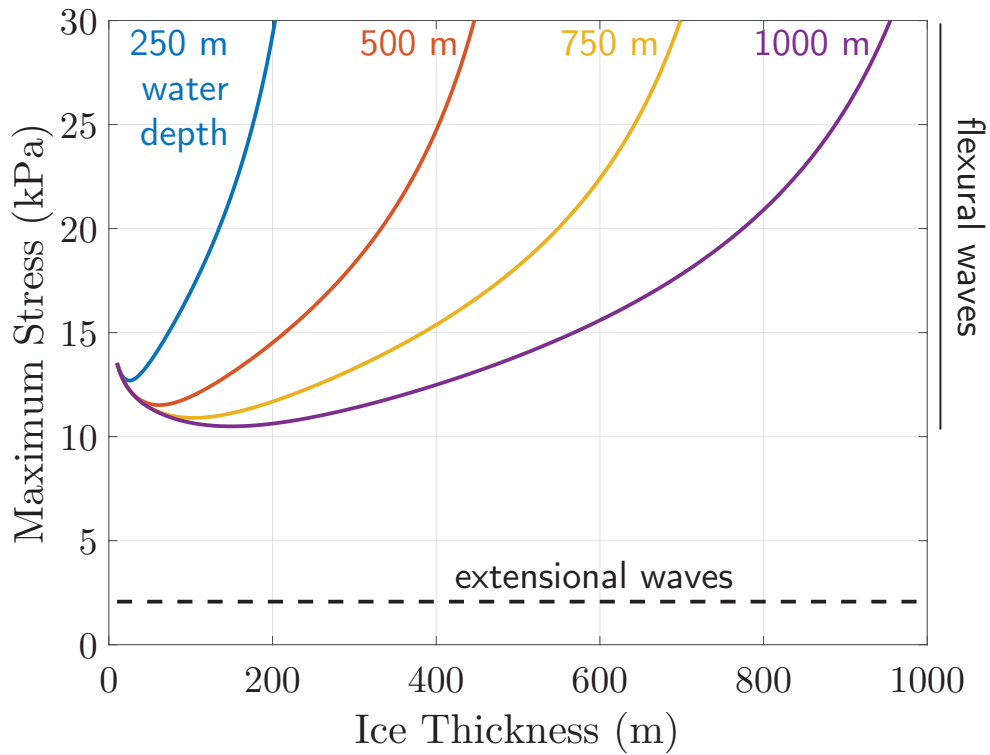
$$\frac{\omega}{k} = \sqrt{\frac{E'}{\rho}}. \quad (9)$$

260 This phase velocity is the plane strain equivalent of the wave speed in a one-dimensional
 261 elastic bar, $\sqrt{E/\rho}$. For the material properties of ice (Table 1), this phase velocity is equal
 262 to 3375 m/s. The extensional mode does not exhibit any ice-ocean interaction (Appendix A).
 263 As was also the case for flexural-gravity waves, this dispersion relation is only valid for
 264 waves with wavelength greater than the ice thickness (Appendix B).

The extensional mode has σ_{xx} -to- u_x impedance component,

$$Z_{xxx}^E = \frac{\Sigma_{xx}}{(-i\omega)U_x} \approx -\sqrt{\frac{2\rho\mu}{1+\nu}}. \quad (10)$$

265 For the material properties of ice $Z_{xxx}^E \approx 2.07$ kPa/(mm/s). This value differs from the
 266 corresponding S-wave impedance by a factor of $\sqrt{2/(1+\nu)} \approx 1.23$.



252 **Figure 4.** Maximum ice shelf stresses generated in response to waves with 0.5 mm/s particle velocity
 253 amplitude. To simulate the effect of ice shelf thinning, curves are calculated for constant ocean floor depth
 254 $H + (\rho/\rho_w)h$ but variable ice thickness h . Stresses refer to the bending stress for flexural waves and the exten-
 255 sional stress for extensional waves. The maximum stress is calculated for each geometry over all wavelengths
 256 λ . The highest flexural wave stress occurs for waves with wavelength λ near the flexural gravity wavelength
 257 λ_{fg} (see Figure 3a).

267 Extensional stresses, denoted σ_e , may be calculated from a horizontal component
 268 velocity seismogram $v_x(t) = \partial u_z / \partial t$ as a simple time domain multiplication,

$$\sigma_e(t) \equiv \sigma_{xx}(t) = Z_{xxx}^E v_x(t). \quad (11)$$

271 4 Fracture Mechanics

272 I analyze brittle fracture using the energy-based Griffith fracture criterion [Griffith,
 273 1921] expressed in terms of the stress concentration at the rift tip [Irwin, 1957]. In this
 274 description, a preexisting fracture will grow in length when its associated stress intensity
 275 factor K exceeds a critical value K_c called fracture toughness, a material property. For
 276 ice, K_c ranges between $150 \text{ kPa}\sqrt{\text{m}}$ and $400 \text{ kPa}\sqrt{\text{m}}$ [Rist *et al.*, 2002]. In Section 6.4 I
 277 discuss the uncertainties associated with fracture toughness values.

278 The model developed in this section depicts the scenario where an ice shelf rift is
 279 loaded by wave-induced ocean stresses that are fast enough to be elastic but slow enough
 280 that inertia is negligible. As stresses increase over a wave period of tens to hundreds of
 281 seconds, the stress concentration at the rift tip increases. Once $K > K_c$, rift tip propa-
 282 gation occurs. In contrast to the loading stage, rift tip propagation may occur sufficiently
 283 rapidly so that the rate of propagation becomes limited by the inertia of the ice. Before
 284 proceeding with this treatment in Section 4.1, I make two technical notes.

285 First, I note that inertia is negligible for perturbations with phase velocities far be-
 286 low the elastic waves speeds (see Appendix A). Such perturbations are called quasi-static
 287 to reflect that they are time dependent but have negligible inertial influence. In Appendix B,
 288 I demonstrate that the quasi-static approximation is valid for ice shelf flexural waves but
 289 not for extensional waves because long period extensional waves are not quasi-static. Treat-
 290 ing the initiation of propagation as quasi-static is nonetheless a reasonable approximation
 291 for the data considered in this paper, however, because in Section 5, I show that flexural
 292 stresses are much larger than extensional stresses and therefore are more likely to be re-
 293 sponsible for the onset of rift propagation.

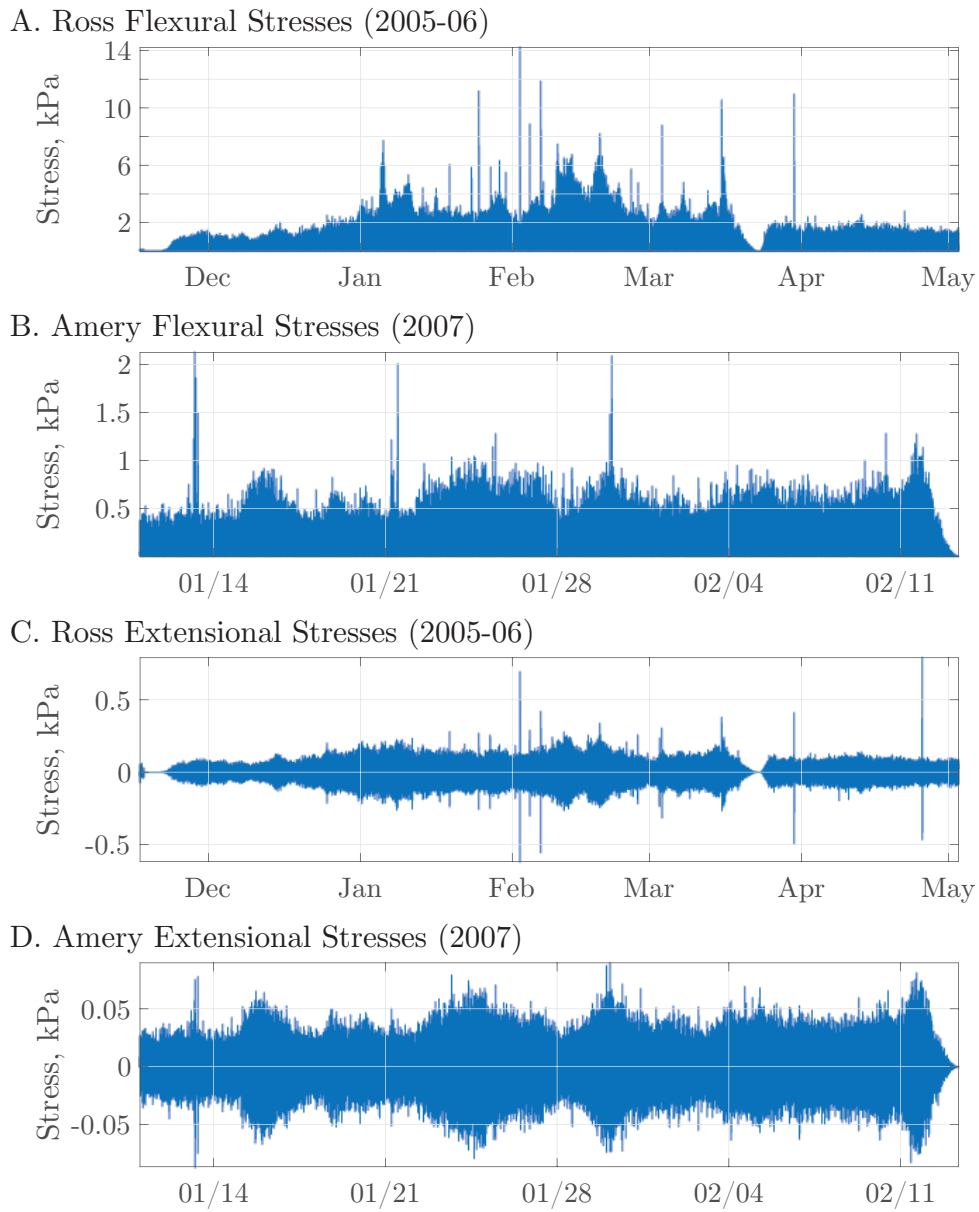
294 Second, I note that the applicability of linear elastic fracture mechanics rests on the
 295 condition of small scale yielding. Before continuing I verify this condition. Small scale
 296 yield occurs when all dimensions of a fractured object are much greater than the dimen-
 297 sion of the plastic region surrounding the rift tip. An estimate of the plastic region size
 298 for an ideally elastic-plastic material is [Broek, 2012] $(K_c / \sigma_y)^2$, where $K_c \approx 100 \text{ kPa}$
 299 $\text{m}^{1/2}$ is the fracture toughness of ice [Rist *et al.*, 2002] and $\sigma_y \approx 100 \text{ kPa}$ is the yield
 300 stress of ice [Van der Veen, 1998]. These estimates give a critical flaw size of about 1 m.
 301 Using a larger fracture toughness of $K_c \approx 400 \text{ kPa m}^{1/2}$ gives plastic zone size 16 m. For
 302 typical ice shelf thicknesses of one to several hundred meters we may safely proceed with
 303 a plane strain fracture mechanics treatment.

304 4.1 The onset of propagation

305 For a fixed geometry, the stress intensity factor is a linear functional of the stress
 306 tensor. The combined effects of background glacial loading and waves may therefore be
 307 treated by superposition,

$$K = K_{\text{glacial stresses}} + K_{\text{waves}}. \quad (12)$$

308 I treat the situation where the rift stress intensity factor K due to glacier stresses is
 309 lower than the fracture toughness $K < K_c$. This is a reasonable assumption for rifts which
 310 are dormant because under linear elastic fracture mechanics, a crack is expected to have
 311 zero propagation if and only if the stress intensity factor is below the fracture toughness
 312 $K < K_c$. The catalog of rifts published by Walker *et al.* [2013] shows that the majority
 313 of Antarctic rifts are dormant, thus suggesting that the analysis developed here applies



269 **Figure 5.** Calculated wave stresses on the Ross and Amery Ice Shelves. Note the different horizontal and
 270 vertical axes.

314 to the majority of Antarctic rifts. For simplicity, I assume that $K_{\text{glacial stresses}} \approx 0$. Rift
 315 propagation would occur at a lower stress than predicted if $K_{\text{glacial stresses}} > 0$.

316 The stress intensity factor due to wave motion may then be broken into flexural and
 317 extensional components,

$$K \approx K_{\text{extension}} + K_{\text{flexure}}. \quad (13)$$

318 The stress intensity factor due to extensional motion is [Broek, 2012],

$$K_{\text{extension}} = \sigma_e \sqrt{\pi L/2}. \quad (14)$$

319 The stress intensity factor due to bending of a buoyantly floating plate is [Bažant,
 320 1992],

$$K_{\text{flexure}} = |\sigma_f| \sqrt{\pi \lambda_{fg}}, \quad (15)$$

321 where the flexural-gravity wavelength is defined in Equation 5. This stress intensity factor
 322 for bending of a floating plate is valid for rifts that are longer than the flexural-gravity
 323 wavelength.

324 4.2 Inertial effects during rift tip propagation

325 The rapid propagation of fractures requires accounting for elastodynamic effects. *Freund*
 326 *[1972a,b]* was the first to generalize the analysis of *Irwin [1957]* to the elastodynamic
 327 case. He found that the stress intensity factor may be written as the product of static and
 328 dynamic terms,

$$K(L, \dot{L}) = \kappa(\dot{L}) K_0(L), \quad (16)$$

329 where an overdot denotes a time derivative. Here, $K_0(L)$ is the time-independent stress
 330 intensity factor, which is identical to the stress intensity factor that would occur due to
 331 loading of a rift with instantaneous length L . The function κ has its origin in a particular
 332 elastodynamic transfer function, and is well approximated by

$$k(\dot{L}) \approx 1 - \frac{1}{c_r} \frac{\partial L}{\partial t}, \quad (17)$$

333 where c_r is the Rayleigh wave speed in ice. The conditions under which Equation 16 is
 334 valid are quite general [Freund, 1998; Rice, 2001]. Specifically, the existence of the fac-
 335 torization of the stress intensity factor into static and dynamic parts is independent of geo-
 336 metric and loading configuration.

337 Combining Equations 16 and 17 gives the rift tip equation of motion

$$\frac{\partial L}{\partial t} = \begin{cases} c_r \left[1 - \left(\frac{K_c}{K} \right)^2 \right] & K \geq K_c \\ 0 & K < K_c \end{cases} \quad (18)$$

338 This result has general features which have been noted previously [Freund, 1998], but are
 339 worth highlighting. In particular, the crack tip velocity has an instantaneous dependence
 340 on the stress level through the stress intensity factor K . This instantaneous response re-
 341 sults because there is no sensitivity to the second derivative of L in Equation 18. Integrat-
 342 ing the rift tip velocity gives the rift propagation distance,

$$\delta L(t) = c_r \int_0^t \left\{ 1 - \frac{K_c [L(t')]}{K[\sigma(t'), L(t')]} \right\} dt'. \quad (19)$$

343 I note that this description accounts for spatial variability in fracture toughness due, for
 344 example, to the presence of high toughness suture zones with accreted basal marine ice
 345 [Holland et al., 2009; McGrath et al., 2012; Jansen et al., 2013; LeDoux et al., 2017].

5 Analysis of seismic data from the Ross and Amery Ice Shelves

5.1 Wave-induced stresses

Using the data described in Section 2.2, I estimate flexural stresses σ_f using Equation 7 and extensional stresses σ_e using Equation 11. There are two primary results (Figure 5). First, wave stresses are much greater on the Ross Ice Shelf than on the Amery Ice Shelf. Second, on both the Amery and the Ross Ice Shelf, flexural waves carry greater stresses than extensional waves. These two patterns are true of the peak stresses as well as the root mean squared (RMS) averaged stresses. The largest observed flexural and extensional stresses on the Ross Ice Shelf were 14.2 and 0.8 kPa, respectively. On the Amery Ice Shelf, the largest observed flexural and extensional stresses were 2.1 and 0.09 kPa, respectively. The RMS flexural and extensional stresses on the Ross Ice Shelf were 0.6 kPa and 0.03 kPa. The RMS flexural and extensional stresses on the Amery were 0.2 kPa and 0.01 kPa.

The most likely reason for the higher observed wave stresses on the Ross Ice Shelf compared to the Amery is that the Ross seismograms are much longer (167 d) than the Amery seismograms (36 d) and were therefore able to record a wider range of variability in ocean wave activity. To test this hypothesis, I examine the most quiet period during the Ross deployment, December 2005. I refer to this as the Ross quiet period. I find that the wavefield stresses during the Ross quiet period were similar to those on the Amery Ice Shelf. During the Ross quiet period, the maximum inferred flexural and extensional stresses were 2.0 kPa and 0.13 kPa, respectively.

Flexural waves carried greater stresses than extensional waves during the two observation periods. The Ross Ice Shelf wave field had extensional waves with greater particle velocity amplitude than flexural wave particle velocity amplitude by a factor of three [Bromirski *et al.*, 2010, 2015, 2017]. These two waves, however, have different wave impedances. As a result, the larger stress need not be caused by the larger particle velocity.

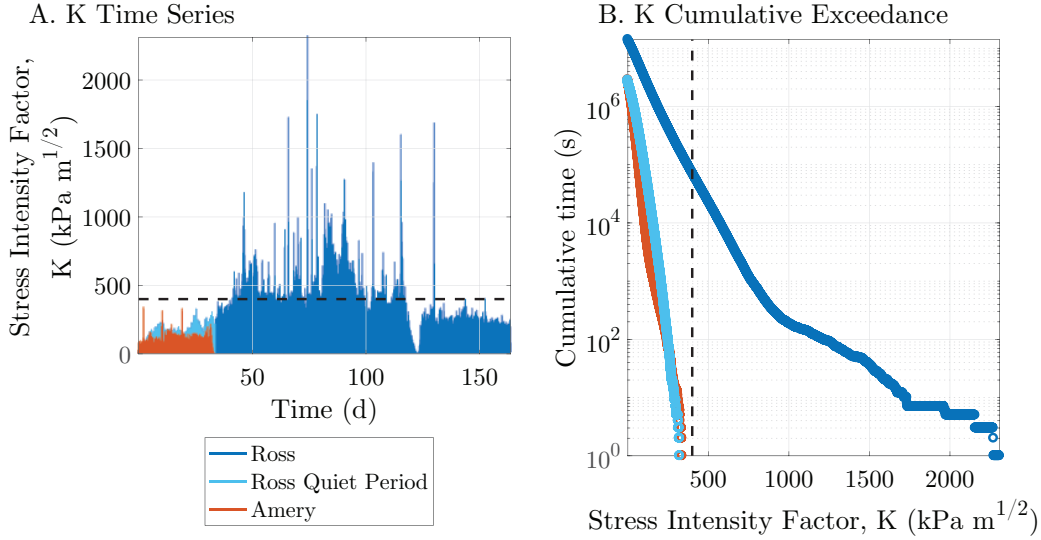
5.2 Rift propagation

Using the estimated stresses, I calculate the stress intensity factor K using Equation 13. There are two main results. The first result is that waves stresses were exceeded the fracture criterion on the Ross Ice Shelf but not on the Amery Ice Shelf (Figure 6). As discussed later (Section 6.4), I assume a fracture toughness $K_c = 400 \text{ kPa}\sqrt{\text{m}}$ to represent tough suture zones with accreted basal marine ice. With this fracture toughness, I predict that rift propagation was possible for a cumulative total of $\sim 10^4$ s during the Ross Ice Shelf observation period. On the Amery Ice Shelf and during the quiet period on the Ross Ice Shelf, I predict that wave stresses were not large enough to induce propagation.

The second result is that, in the absence of any other resistance to rift propagation, the inferred wave-induced stresses are predicted to have caused much more propagation than was actually observed. I use the integral in Equation 19 to calculate rift tip propagation distances. On the Ross Ice Shelf, a fracture toughness $K_c = 400 \text{ kPa}\sqrt{\text{m}}$ results in a physically unrealistic 10^6 km of rift tip propagation. Actual rift propagation was measured to have been less than 1 km during the observation period (Section 2). Motivated by this discrepancy, I next consider several possible sources of resistance to ice shelf rift propagation.

5.3 Rift cohesive strength

In order to match the observed lack of rift propagation, I consider two additional types of rift strength. First, I consider the situation discussed by Bassis *et al.* [2007] where the fracture toughness experiences an increase by an amount Δ to a new value $K_c + \Delta$. This perturbed value could equally well represent fracture toughness variation in space or



372 **Figure 6.** Comparison of the wave-induced stress intensity factor on the Ross (blue) and Amery (red) Ice
 373 Shelves. During the time of minimal wave activity on the Ross Ice Shelf (light blue), wave stresses were
 374 comparable to those observed on the Amery Ice Shelf. The stress intensity factor was computed from seis-
 375 mograms using Equation 13 and does not account for cohesive strengthening (Section 5.3). The dashed
 376 lines shows the fracture toughness K_c and therefore the value of the stress intensity factor K at which rift
 377 propagation is predicted to occur.

400 in time. Returning to the calculation in the previous section, I find that a value of $\Delta =$
 401 $1600 \text{ kPa}\sqrt{\text{m}}$ is necessary to match the observation that less than 1 km of propagation
 402 occurred. This value results in a total ice fracture toughness $\sim 2 \text{ MPa}\sqrt{\text{m}}$, which is an
 403 order of magnitude higher than typical laboratory-derived values [Rist *et al.*, 2002]. For
 404 this reason, I consider variable fracture toughness to not be a viable mechanism to explain
 405 the observed rift behavior.

406 As a second strengthening mechanism, I consider the cohesive effect of refrozen
 407 melange and sea ice between the rift walls. The stress intensity factor due to a uniformly
 408 applied stress acting to resist rift opening is the same as in Equation 14 but with opposite
 409 sign [Sih, 2012],

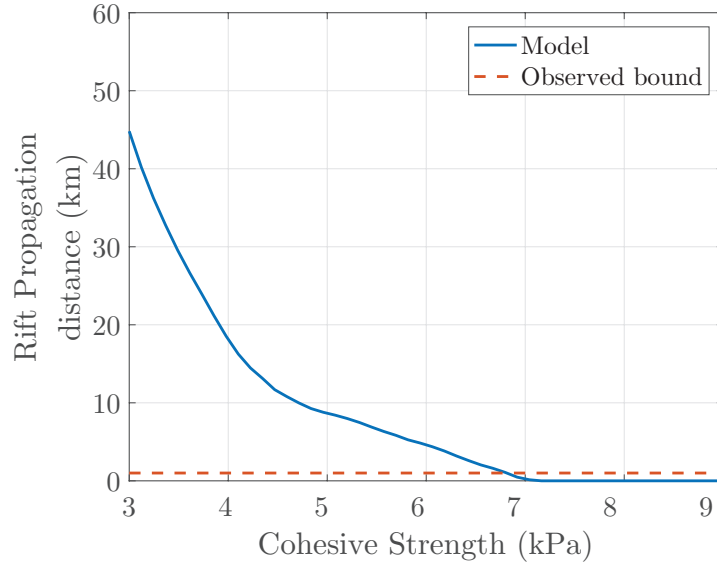
$$K_{\text{cohesion}} = -\sigma_c \sqrt{\pi L/2}, \quad (20)$$

410 where σ_c is defined here to be the stress due to cohesive melange and sea ice that act to
 411 “glue” the rift walls together. Equation 13 then becomes,

$$K \approx \max [K_{\text{extension}} + K_{\text{flexure}} + K_{\text{cohesion}}, 0]. \quad (21)$$

412 The maximum function is applied because the cohesive strength does not result in a neg-
 413 ative stress intensity factor K . A negative K would imply closing motion of the rift walls.
 414 Instead, a cohesive stress is generated only in response to wave stresses and therefore
 415 never results in negative K .

416 I find that a cohesive stress $\sigma_c = 6.8 \text{ kPa}$ is the minimum required cohesive stress
 417 necessary to produce $\delta L < 1 \text{ km}$. This result is plotted in Figure 7, which plots the pre-
 418 dicted amount of rift propagation as a function of the cohesive strength of the rift. In the
 419 Section 6.5 I discuss several interpretations of this cohesive stress.



420 **Figure 7.** The predicted rift propagation decreases as the rift cohesive strength increases. Satellite imagery
 421 shows less than 1 km of propagation, therefore suggesting a cohesive strength of 6.8 kPa. The blue curve was
 422 calculated using Equations 19 and 21.

423 6 Discussion and Conclusions

424 6.1 Uncertainties in the calculation of wave-induced stresses

425 I have calculated ice shelf stresses from seismic data and related these stresses to
 426 a fracture criterion. Although I have made several simplifying assumptions, the stresses
 427 that I estimate are nevertheless in reasonable agreement with previous studies. *Sergienko*
 428 [2017] for example, used the BEDMAP2 geometry from the Ross Ice Shelf but employing
 429 an idealized wave forcing, calculated flexural stresses in the range of 0-15 kPa. In compar-
 430 ison, I find a RMS and peak wave stress on the Ross Ice Shelf of 0.8 and 17.5 kPa. The
 431 principal differences from the results of *Sergienko* [2017] are related topographic focus-
 432 ing. I treat a simplified two-dimensional geometry where the ice shelf is infinitely long
 433 and wide, small ice shelves of comparable dimension to the flexural gravity length scale
 434 are expected to significantly deviate from the predictions made in this paper. One reason
 435 for this is that tidal stresses, for example, become significant within a distance from the
 436 grounding line that scales with λ_{fg} [*Holdsworth, 1969; Vaughan, 1995*].

437 6.2 Can ocean waves trigger rift propagation?

438 To the best of my knowledge, no previous study has definitively demonstrated that
 439 ocean waves may trigger ice shelf rift propagation. To address this situation, I have at-
 440 tempted in this paper to construct a simple model of wave-induced rifting. Although I
 441 have been able to make this model behave in a manner consistent with observed rift be-
 442 havior, no large rift propagation event occurred during the period from which I have data.
 443 As a result, definitive proof of ocean wave triggering remains elusive. This result empha-
 444 sizes the importance of ongoing seismological fieldwork on ice shelves [*Banwell et al.,*
 445 *2017; Bromirski et al., 2017*]. Additional fieldwork would clarify other issues as well. Al-
 446 though I show that a period of low wave activity on the Ross is comparable to the Amery
 447 record, further observations are needed to confirm whether activity on the Amery –or any

448 other ice shelf for that matter— ever reaches stress levels as high as those observed on the
449 Ross.

450 **6.3 Other mechanisms of episodic rift extension**

451 *Larour et al.* [2004a], citing laboratory studies such as those by *DeFranco and Dempsey*
452 [1994], invokes constitutive instability as a possible mechanism for episodic rift activity.
453 Constitutive instability gives rise, for example, to the stick-slip instability that is respon-
454 sible for basal stick slip motion of glaciers and ice sheets [*Lipovsky and Dunham*, 2016,
455 2017]. Such behavior is a typical pathology of laboratory experiments conducted on sam-
456 ples which are too thin to achieve a state of plane strain [*Bažant*, 1993; *Broek*, 2012]. As
457 discussed in Section 4, ice shelf rifts are expected to occur in ice that is thick enough to
458 be in plane strain. This type of behavior is therefore expected to occur in thinner bodies
459 of floating ice such as sea ice [*DeFranco and Dempsey*, 1994]. Furthermore, a constitutive
460 instability hypothesis is appealing in situations such as the tectonic earthquake cycle where
461 the loading applied to a system is known to be approximately constant in time. The find-
462 ing from the present study, that wave-induced loading is highly time dependent, suggests
463 that constitutive instability, though possible, is not a strictly necessary condition to explain
464 episodes of ice shelf rift propagation.

465 **6.4 The fracture toughness of ice shelf suture zones**

466 I have chosen a value $K_c = 400 \text{ kPa}\sqrt{\text{m}}$ to represent the fracture toughness of ice
467 shelf suture zones. This choice is based on the best available laboratory data [*Rist et al.*,
468 2002], and was chosen to be at the high end of laboratory data to reflect the fact that su-
469 ture zones appear to be more resistant to rift propagation than the surrounding ice shelf
470 [*Holland et al.*, 2009; *McGrath et al.*, 2012; *Jansen et al.*, 2013; *LeDoux et al.*, 2017]. I
471 also invoke the laboratory measurements to support the claim that fracture toughness vari-
472 ations cannot entirely be responsible for the observed response of the Nascent Iceberg Rift
473 to wave-induced stresses. An important caveat to these statements is that, to my knowl-
474 edge, no ice core has ever been collected from an ice shelf suture zones. Fracture tough-
475 ness measurements from *in situ* suture zone ice cores could therefore support or refute
476 these ideas. The exact micromechanical processes that result in the apparently elevated
477 fracture tough of ice shelf suture zones remain unknown [*McGrath et al.*, 2014].

478 **6.5 Cohesive rift strengthening**

479 My description of rift propagation mechanics predicts that wave stresses would have
480 caused calving of a tabular iceberg in the absence of additional sources of rift strength.
481 Previous studies have suggested a role for melange dynamics as a rift strengthening mech-
482 anism [*MacAyeal et al.*, 1998; *Rignot and MacAyeal*, 1998; *Larour et al.*, 2004b; *Fricker*
483 *et al.*, 2005]. For simplicity I have quantified this stabilizing tendency as a force applied
484 uniformly over the entire rift length. This rift strengthening can equivalently be thought
485 of as a cohesive zone [*Rice*, 1968]. I have not attempted to quantify the spatial variation
486 of rift strengthening; it may be the case that rift strengthening is localized to the near-tip
487 region [*Dugdale*, 1960; *Barenblatt*, 1962]. Near-tip localization of cohesive strength to a
488 process-zone region [*Broek*, 2012] could result from the effect of bottom crevasses form-
489 ing ahead of the rift tip [*Rice and Levy*, 1972] or because of rift tip blunting [*Larour et al.*,
490 2004b].

491 **6.6 Response to warming, melting, and thinning**

492 The rift model presented here suggests at least three different effects related to ice
493 shelf warming and thinning. First, the result of Section 5.3 suggests that rift-filling melange
494 plays an important role in stabilizing rift propagation. Reduced melange extent will there-

495 fore weaken ice shelves by destabilizing rift propagation [*Rignot and MacAyeal*, 1998;
 496 *MacAyeal et al.*, 1998]. Second, as proposed by *Holland et al.* [2009] and *McGrath et al.*
 497 [2014], submarine melting of tough basal marine ice may lower the depth-integrated frac-
 498 ture toughness and therefore destabilize rift propagation. Melting and warming are there-
 499 fore generally expected to be destabilizing.

500 The wave response to thinning, in contrast, is stabilizing. Stabilization occurs for
 501 two reasons. First, the flexural-gravity wavelength (Equation 5) is expected to decrease.
 502 This results in a lower stress concentration due to flexural waves (Equation 15). Second,
 503 the flexural wave impedance is an increasing function of ice thickness (Figure 4). Thus
 504 thinning of an ice shelf is expected to lower wave stresses. Both of these stabilizing ef-
 505 fects occur because thin ice shelves are more compliant and more compliant structures are
 506 less susceptible to brittle fracture. Further observations, both seismic and remotely sensed,
 507 are needed to quantify whether the destabilization due to melting and warming is greater
 508 than the stabilization due to thinning.

509 **6.7 The Loose Tooth Rift: stabilization due to propagation into deeper water?**

510 The location where the Loose Tooth T2 Rift intersects the ice front, i.e. where the
 511 rift initiated, occurs in a part of the shelf that is above shallow water ($H = 253$ m).
 512 The rift has subsequently propagated into a part of the shelf that is above deeper water
 513 ($H = 466$ m). The ice thickness at the front is similar to the ice thickness at the current
 514 rift tip ($h = 265$ m versus $h = 301$ m). Carrying out a calculation of maximal flexu-
 515 ral stress similar to Figure 4, I find that waves with identical particle velocity amplitudes
 516 would induce stresses approximately 27% higher at the ice front versus the current rift
 517 tip. Observed wave-induced stresses on the Amery were very near the failure criterion
 518 (Figure 6b). This result suggests that the Loose Tooth T2 Rift was more susceptible to
 519 wave-induced stresses during its initial formation in shallow water, and that propagation
 520 into deeper water may have stabilized the rift tip in its current position. As noted above,
 521 this hypothesis is not strictly testable because there were no seismometers deployed on the
 522 Amery during the initial formation of the Loose Tooth T2 Rift. Future seismic deploy-
 523 ments would therefore be useful because they could clarify whether stabilization due to
 524 propagation into deeper water is an important process.

525 **6.8 Summary and Conclusions**

526 I propose a simple rift propagation criterion based on the observation that most ice
 527 shelf rifts show extended periods of dormancy and therefore must have low background
 528 stress concentrations. This low background stress concentration makes ice shelf rifts sus-
 529 ceptible to wave-induced stresses. I infer that a cohesive strengthening of the rift, possibly
 530 due to refrozen melange, counteracts this destabilizing tendency. I relate this description
 531 of rift propagation to *in situ* ice shelf stresses inferred using passive seismology. By infer-
 532 ring stresses associated with rift propagation, this work addresses a basic limitation in our
 533 understanding glacier calving physics: specifically, knowledge of the state of stress at the
 534 site of fracture [*Benn et al.*, 2007]. This study therefore offers a detailed glimpse into the
 535 mechanics of a particular type of glacier calving, ice shelf rift propagation.

536

A: Governing Equations

537

538

539

540

541

542

The propagation of ocean waves in floating ice shelves has received extensive treatment. The flexural motions of an elastic bar were first examined by *Greenhill* [1886]. This analysis was generalized to extensional motions by [*Press and Ewing*, 1951, but see also literature cited therein]. The main reason that I repeat the analysis of [*Press and Ewing*, 1951] is to obtain self-consistent expressions for the particle velocities, stresses, and dispersion relations that were not explicitly given by [*Press and Ewing*, 1951].

543

A.1 The elastic ice layer

I consider a coordinate system with the z direction being positive upwards and x being positive in the direction of ice flow. An ice layer that is initially at rest and everywhere at overburden pressure occupies the region between $z = 0$ and $z = -h$. The entire geometry is assumed to be translationally invariant in the x direction, and I take $u_y = \partial/\partial y = 0$ so that deformations are in a state of plane strain. Perturbations to this initial state obey the momentum balance equations,

$$\rho \frac{\partial^2 u_x}{\partial t^2} = \frac{\partial \sigma_{xx}}{\partial x} + \frac{\partial \sigma_{xz}}{\partial z}, \quad (\text{A.1})$$

$$\rho \frac{\partial^2 u_z}{\partial t^2} = \frac{\partial \sigma_{xz}}{\partial x} + \frac{\partial \sigma_{zz}}{\partial z}, \quad (\text{A.2})$$

544

545

for ice density ρ and stress tensor σ_{ij} . Stresses are related to displacement gradients through the constitutive relationship [*Malvern*, 1969],

$$\sigma_{ij} = \lambda \left(\frac{\partial u_k}{\partial x_k} \right) \delta_{ij} + \mu \left(\frac{\partial u_i}{\partial x_j} + \frac{\partial u_j}{\partial x_i} \right), \quad (\text{A.3})$$

546

547

where, for simplicity, elastic anisotropy is neglected. The values of elastic moduli, here written using Lamé's parameter λ and the shear modulus μ , are given in Table 1.

Applying the transform of Equation 2 to the governing equations (Equations A.1-A.3) gives rise to a system of two coupled ordinary differential equations with derivatives in z . These equations have solution [*Graff*, 2012],

$$U_x = ik (A \sin \alpha z + B \cos \alpha z) + i\beta (C \cos \beta z - D \sin \beta z), \quad (\text{A.4})$$

$$U_z = \alpha (A \cos \alpha z - B \sin \alpha z) + k (C \sin \beta z + D \cos \beta z), \quad (\text{A.5})$$

where,

$$\alpha = k \sqrt{\left(\frac{\omega}{kc_p} \right)^2 - 1}, \quad (\text{A.6})$$

$$\beta = k \sqrt{\left(\frac{\omega}{kc_s} \right)^2 - 1}. \quad (\text{A.7})$$

548

549

Here, c_p and c_s are the p- and s-wave speeds in the ice (see Table 1). The quasi-static limit occurs when $\omega/(kc_p) \ll 1$ and $\omega/(kc_s) \ll 1$. In this case $\alpha \approx \beta \approx k$.

The boundary conditions at the ice-atmosphere boundary $z = 0$, are

$$\sigma_{xz}(z = 0) = 0, \quad (\text{A.8})$$

$$\sigma_{zz}(z = 0) = 0. \quad (\text{A.9})$$

550

Two other boundary conditions are required, and these occur at the ice-ocean interface.

551

A.2 Ice–ocean coupling

552

553

The unperturbed ice–ocean interface is located at $z = -h/2$. The ice–ocean boundary moves in response to perturbations, with the deformed interface located at

$$z = -h + \phi(x, t). \quad (\text{A.10})$$

Consistent with a linearized theory of wave propagation, I assume that such geometric changes are small and following standard treatments [*Lipovsky and Dunham, 2015; Gill, 2016*] I prescribe boundary conditions on the undeformed interface. At this boundary, the force exerted on the ice by the water $\delta p(x, t)$ is equal and opposite to the force exerted by the water on the ice σ_{zz} ,

$$\sigma_{zz}(-h) = -\delta p(x, t). \quad (\text{A.11})$$

The ocean is treated as inviscid so there is no shear stress,

$$\sigma_{xz}(-h) = 0. \quad (\text{A.12})$$

And by continuity the velocities must match between the fluid and solid,

$$\frac{\partial u_z}{\partial t}(-h) = v_z, \quad (\text{A.13})$$

554

555

556

where v_z is the vertical fluid velocity. I next examine motions in the sub-ice ocean waters with the goal of describing the fields δp and v_z (Equations A.11 and A.13) on the ice–ocean interface.

557

A.3 Flow in the ocean cavity

558

559

I examine the behavior of perturbations to a sub-ice shelf cavity initially at rest. In this initial state, the pressure in the water is,

$$p_0(z) = \rho_w g(z + h) + \rho_w g h. \quad (\text{A.14})$$

560

I then define the total fluid pressure p' to be

$$p'(x, z, t) = p(x, z, t) + p_0(z) \quad (\text{A.15})$$

Flow perturbations follow the linearized equations for an incompressible, inviscid flow with uniform density. The horizontal and vertical momentum balance equations are

$$\rho_w \frac{\partial v_x}{\partial t} = -\frac{\partial p}{\partial x} \quad (\text{A.16})$$

$$\rho_w \frac{\partial v_z}{\partial t} = -\frac{\partial p}{\partial z}. \quad (\text{A.17})$$

561

562

563

Here v_x and v_z are the x - and z -components of fluid velocity. The statement of mass conservation may be combined with Equations A.16 and A.17 with the result being Laplace's equation for pressure *Gill* [2016],

$$\nabla^2 p = 0. \quad (\text{A.18})$$

564

565

The boundary condition at the ocean bottom, $z = -h - H$, is that vertical velocities vanish,

$$v_z(z = -h - H) = 0. \quad (\text{A.19})$$

566

567

568

At the ice–ocean interface, the water pressure perturbation is approximately equal to the hydrostatic pressure at the deformed ice–ocean interface location ϕ plus the pressure exerted by the ice on the water,

$$p(-h) = \rho_w g \phi(x, t) + \delta p(x, t). \quad (\text{A.20})$$

The fluid equations (A.18-A.20) may be solved in the transform domain using Equation 2. The result is a transfer function between ΔP and surface height Φ ,

$$\Delta P = \rho_w g \left(\frac{\omega^2}{gk} \coth(kH) - 1 \right) \Phi \equiv -T(k, \omega) \Phi. \quad (\text{A.21})$$

I again apply the convention from the main text that capital letters denote Fourier transformed quantities.

The transfer function of Equation A.21, combined with the the ice–ocean coupling conditions (Equations A.11 and A.13), allows me to write the entire coupled ice–ocean problem exclusively in terms of boundary conditions on the elastic solid. In Equation A.21, ΔP and Φ can be eliminated in favor of the field variables Σ_{zz} and U_z , defined in the elastic solid. The result is the bottom boundary conditions on the elastic ice layer,

$$\Sigma_{zz}(z = -h) = T(k, \omega) U_z(z = -h), \quad (\text{A.22})$$

$$\Sigma_{xz}(z = -h) = 0. \quad (\text{A.23})$$

It is interesting to note that ice–ocean coupling manifests itself as the condition in Equation A.22, namely, as a Robin type boundary condition that relates the vertical elastic displacement to the vertical compressive elastic stress.

A.4 The dispersion relation

The four boundary conditions (Equations A.8, A.9, A.22, and A.23) on the elastic solid result in a homogeneous system of equations,

$$\left\{ \begin{array}{cccc} 2(k^2 - \beta^2) \mu \cos(h\alpha) & 4k\beta\mu \cos(h\beta) & 0 & 0 \\ 2k\alpha \sin(h\alpha) & (\beta^2 - k^2) \sin(h\beta) & 0 & 0 \\ 0 & 0 & 4k\beta\mu \sin(h\beta) & 2(\beta^2 - k^2) \mu \sin(h\alpha) \\ 0 & 0 & (k^2 - \beta^2) \cos(h\beta) & 2k\alpha \cos(h\alpha) \end{array} \right\} -T \left[\begin{array}{cccc} \alpha \sin(h\alpha) & -k \sin(h\beta) & k \cos(h\beta) & \alpha \cos(h\alpha) \\ 0 & 0 & 0 & 0 \\ \alpha \sin(h\alpha) & -k \sin(h\beta) & k \cos(h\beta) & \alpha \cos(h\alpha) \\ 0 & 0 & 0 & 0 \end{array} \right] \begin{pmatrix} B \\ C \\ D \\ A \end{pmatrix} = \begin{pmatrix} 0 \\ 0 \\ 0 \\ 0 \end{pmatrix} \quad (\text{A.24})$$

Solutions to these equations require a vanishing determinant, and this condition gives rise to the dispersion relation,

$$D(k, \omega) = D_E(k, \omega) D_F(k, \omega) + D_{HD}(k, \omega) = 0. \quad (\text{A.25})$$

where,

$$D_F \equiv \frac{\tan(\alpha h)}{\tan(\beta h)} + \frac{(k^2 - \beta^2)^2}{4\alpha\beta k^2}, \quad (\text{A.26})$$

$$D_E \equiv \frac{\tan(\alpha h)}{\tan(\beta h)} + \frac{4\alpha\beta k^2}{(k^2 - \beta^2)^2}, \quad (\text{A.27})$$

$$D_{HD} \equiv \frac{T}{2\mu} \frac{\alpha(\beta^2 + k^2) [\tan^2(\alpha h) - 1]}{4\alpha\beta k^2 \tan(\beta h)} \left[\frac{\tan^2(\beta h) - 1}{\tan^2(\alpha h) - 1} + \frac{\tan(\alpha h)}{\tan(\beta h)} \frac{4\alpha\beta k^2}{(k^2 - \beta^2)^2} \right]. \quad (\text{A.28})$$

The subscript *HD* stands for hydrodynamic. Terms with this subscript are related to flow in the sub shelf cavity.

When ice–ocean coupling is absent, $T = 0$ and so $D_{HD} = 0$. In this case Equation A.25 reduces to the Lamb wave dispersion relation. This dispersion relation corresponds to the motions of an elastic layer with zero stress boundary conditions [*Graff*,

582 2012]. The Lamb wave dispersion relation is notable because it consists of uncoupled
 583 flexural and extensional modes. Mathematically this uncoupling occurs because it is possible
 584 to factor the dispersion relation into the product of two terms, D_E and D_F . Equation
 585 A.25 is equivalent to Equation 49 of *Wang and Shen* [2010] in the case of a perfectly
 586 elastic ice layer.

587 In general, the mechanical interaction that occurs at the ice–ocean interface results
 588 in coupling between the flexural and extensional motions of the ice shelf. For this reason,
 589 there are no longer uncoupled flexural and extensional modes over the entire frequency-
 590 and wavenumber-spectra as there is in the more specific Lamb wave case. I will show in
 591 the next section, however, that for wavelengths that are long compared to the ice thickness,
 592 a simplification to extensional and flexural modes occurs.

593 **B: The long wavelength limit**

I calculate the Taylor series in the small parameter kh for the dispersion relation of Equation A.25,

$$D_F \approx \frac{1}{12} \left(\frac{\omega}{kc_s} \right)^2 \left\{ \frac{\omega^2}{c_s^2 k^2} \left[\frac{1}{2} (\gamma^2 - 1)^2 h^2 k^2 - 3 \right] + (\gamma^2 - 1) h^2 k^2 \right\}, \quad (\text{B.1})$$

$$D_E \approx \frac{1}{4} \left(\frac{\omega}{kc_s} \right)^2 \left[4 (\gamma^2 - 1) + (2\gamma^4 - 1) \frac{\omega^2}{c_s^2 k^2} \right], \quad (\text{B.2})$$

$$D_{HD} \approx \frac{T}{\mu h k^2} \frac{1}{4} \left(\frac{\omega}{kc_s} \right)^4 \left[4 (\gamma^2 - 1) + (2\gamma^4 - 1) \frac{\omega^2}{c_s^2 k^2} \right] \left[\frac{\gamma^2 + 1}{2} \frac{\omega^2}{k^2 c_s^2} + 1 \right]. \quad (\text{B.3})$$

I have defined $\gamma \equiv c_s/c_p$. The resulting expression for the dispersion relation permits factorization into the form,

$$\begin{aligned} D(k, \omega) \approx & \left(\frac{\omega}{c_s k} \right)^4 \left\{ 4 (\gamma^2 - 1) + (2\gamma^4 - 1) \left(\frac{\omega}{c_s k} \right)^2 \right\} \\ & \times \left\{ (\gamma^2 - 1) h^2 k^2 + \frac{3T}{\mu h k^2} \left[\frac{\gamma^2 + 1}{2} \left(\frac{\omega}{c_s k} \right)^2 + 1 \right] \right. \\ & \left. + \left[\frac{1}{2} (\gamma^2 - 1)^2 h^2 k^2 - 3 \right] \left(\frac{\omega}{c_s k} \right)^2 \right\}, \end{aligned} \quad (\text{B.4})$$

594 which has the property that it consists of two uncoupled modes.

595 The first mode, corresponding to the first curly-bracketed term, is identical to the
 596 long wavelength symmetric Lamb wave mode. Its phase velocity is given by Equation 9.

597 The second mode, corresponding to the second curly-bracketed term, is a modifica-
 598 tion of the long wavelength antisymmetric Lamb wave mode. The dispersion relation for
 599 this mode is,

$$(1 - \gamma^2) h^2 k^2 + \frac{3T}{\mu h k^2} \left[\frac{\gamma^2 + 1}{2} \left(\frac{\omega}{c_s k} \right)^2 + 1 \right] + \left[\frac{1}{2} (\gamma^2 - 1)^2 h^2 k^2 - 3 \right] \left(\frac{\omega}{c_s k} \right)^2 = 0. \quad (\text{B.5})$$

600 Keeping only the lowest order terms in the small parameter kh gives

$$Dk^4 - h\rho\omega^2 = -T, \quad (\text{B.6})$$

601 where $D \equiv \mu(1 - \gamma^2)h^3/3$ is the flexural rigidity, which is equivalent to another commonly
 602 used expression, $Eh^3/[12(1 - \nu^2)]$.

603 I have not yet made use of the ice-ocean transfer function. The results in this section
 604 up to this point are therefore valid for any ice–ocean transfer function T . Using the
 605 transfer function T from Equation A.21 then gives the dispersion equation of Equation 4.

606

C: Wave particle motions

I calculate particle motions by regrouping the general solution (Equations A.4 and A.5) into symmetric and antisymmetric terms. In order to highlight symmetries about the midplane of the ice layer, I define the coordinate $z' \equiv z - h/2$. The ice-atmosphere and ice-ocean surfaces are then located at $z' = \pm h$. These terms correspond to extensional and flexural motions, respectively,

$$\frac{U_x^F}{A} = ik \sin \alpha z' - i \frac{D}{A} \beta \sin \beta z', \quad (\text{C.1})$$

$$\frac{U_z^F}{A} = \alpha \cos \alpha z' + \frac{D}{A} k \cos \beta z', \quad (\text{C.2})$$

$$\frac{U_x^E}{C} = i \frac{B}{C} k \cos \alpha z' + i \beta \cos \beta z', \quad (\text{C.3})$$

$$\frac{U_z^E}{C} = -\frac{B}{C} \alpha \sin \alpha z' + k \sin \beta z'. \quad (\text{C.4})$$

The ratios D/A and B/C are defined from the zero shear stress boundary conditions at $z' = \pm h/2$, as expressed in the second and fourth lines of the matrix in Equation A.24,

$$\frac{B}{C} = \frac{(k^2 - \beta^2) \sin(h\beta/2)}{2k\alpha \sin(h\alpha/2)} \quad (\text{C.5})$$

$$\frac{D}{A} = \frac{2k\alpha \cos(h\alpha/2)}{(\beta^2 - k^2) \cos(h\beta/2)} \quad (\text{C.6})$$

607

The other boundary conditions enter through the requirement that k and ω be related by the dispersion relation. In the long wavelength limit, $B/C \approx D/A \approx -i$. The equations for particle motion (Equations C.1-C.6), combined with the elastic constitutive relation (Equation A.3), suffice to calculate the impedance tensor of Equation 1.

608

609

610

Extensional waves have particle motions,

$$\frac{U_x^E}{C} \approx -2k, \quad (\text{C.7})$$

$$\frac{U_z^E}{C} \approx 2i(kz')k. \quad (\text{C.8})$$

611

I note that the long wavelength limit $kh \ll 1$ is distinct from the quasi static limit where $\omega/(kc_p) \ll 1$. In other words, long wavelength extensional waves are not quasi static. The long wavelength extensional mode has dominantly horizontal displacements $|U_x^E|/|U_z^E| \sim (kz')^{-1}$ that are constant throughout the ice layer. The much smaller vertical displacements, in contrast, are antisymmetric about the midplane of the ice layer.

612

613

614

615

Flexural motions have phase velocity given by Equation 4. The particle motions satisfy,

$$\frac{U_x^F}{A} \approx -\frac{k^2 \omega^2 z'}{2\gamma^2} \quad (\text{C.9})$$

$$\frac{U_z^F}{A} \approx -\frac{ik\omega^2}{2\gamma^2} \quad (\text{C.10})$$

616

Unlike the extensional mode, the flexural mode long wavelength limit is also quasi static.

617

The long wavelength flexural mode has dominantly vertical displacements $|U_z^F|/|U_x^F| \sim (kz)^{-1}$ that are constant throughout the ice layer. The much smaller horizontal displacements, in contrast, are antisymmetric about the midplane of the ice layer.

618

619

620

Acknowledgments

621

This work was supported by a Postdoctoral Fellowship in the Department of Earth and Planetary Sciences at Harvard University. Discussions with Catherine Walker, Jim Rice,

622

623 and Doug MacAyeal provided useful context for this study. Greg Wagner read an early
 624 version of this paper and provided feedback. Victor Tsai demanded better explanations.
 625 Marine Denolle asked several important questions. Olga Sergienko and an anonymous
 626 reviewer provided comments that significantly improved the quality of the manuscript.
 627 All of the data used in this study have been previously published: the seismic data are
 628 freely available at the IRIS Consortium website and the satellite imagery is available on
 629 the NSIDC website. Maps were made using the Antarctic mapping tools for MATLAB
 630 [Greene *et al.*, 2017].

631 References

- 632 Alley, R. B., T. K. Dupont, B. R. Parizek, and S. Anandakrishnan (2005), Access of sur-
 633 face meltwater to beds of sub-freezing glaciers: preliminary insights, *Annals of Glaciol-*
 634 *ogy*, *40*, 8–14.
- 635 Banwell, A. F., I. C. Willis, G. J. Macdonald, B. Goodsell, D. P. Mayer, A. Powell, and
 636 D. R. Macayeal (2017), Calving and rifting on the McMurdo Ice Shelf, Antarctica, *An-*
 637 *nals of Glaciology*, pp. 1–10.
- 638 Barenblatt, G. I. (1962), The mathematical theory of equilibrium cracks in brittle fracture,
 639 in *Advances in Applied Mechanics*, vol. 7, pp. 55–129, Elsevier.
- 640 Bassis, J. N., R. Coleman, H. Fricker, and J. Minster (2005), Episodic propagation of a rift
 641 on the Amery Ice Shelf, East Antarctica, *Geophysical Research Letters*, *32*(6).
- 642 Bassis, J. N., H. A. Fricker, R. Coleman, Y. Bock, J. Behrens, D. Darnell, M. Okal, and
 643 J.-B. Minster (2007), Seismicity and deformation associated with ice-shelf rift propaga-
 644 tion, *Journal of Glaciology*, *53*(183), 523–536.
- 645 Bassis, J. N., H. A. Fricker, R. Coleman, and J.-B. Minster (2008), An investigation into
 646 the forces that drive ice-shelf rift propagation on the Amery Ice Shelf, East Antarctica,
 647 *Journal of Glaciology*, *54*(184), 17–27.
- 648 Bažant, Z. P. (1992), Large-scale thermal bending fracture of sea ice plates, *Journal of*
 649 *Geophysical Research: Oceans*, *97*(C11), 17,739–17,751.
- 650 Bažant, Z. P. (1993), Scaling laws in mechanics of failure, *Journal of Engineering Me-*
 651 *chanics*, *119*(9), 1828–1844.
- 652 Benn, D. I., C. R. Warren, and R. H. Mottram (2007), Calving processes and the dynam-
 653 ics of calving glaciers, *Earth-Science Reviews*, *82*(3), 143–179.
- 654 Borstad, C., A. Khazendar, E. Larour, M. Morlighem, E. Rignot, M. Schodlok, and
 655 H. Seroussi (2012), A damage mechanics assessment of the Larsen B ice shelf prior to
 656 collapse: Toward a physically-based calving law, *Geophysical Research Letters*, *39*(18).
- 657 Borstad, C., E. Rignot, J. Mouginot, and M. Schodlok (2013), Creep deformation and but-
 658 tressing capacity of damaged ice shelves: theory and application to Larsen C ice shelf,
 659 *The Cryosphere*, *7*(6).
- 660 Borstad, C., D. McGrath, and A. Pope (2017), Fracture propagation and stability of ice
 661 shelves governed by ice shelf heterogeneity, *Geophysical Research Letters*, *44*(9), 4186–
 662 4194.
- 663 Broek, D. (2012), *Elementary engineering fracture mechanics*, Springer Science & Busi-
 664 ness Media.
- 665 Bromirski, P., Z. Chen, R. Stephen, P. Gerstoft, D. Arcas, A. Diez, R. Aster, D. Wiens,
 666 and A. Nyblade (2017), Tsunami and infragravity waves impacting Antarctic ice
 667 shelves, *Journal of Geophysical Research: Oceans*.
- 668 Bromirski, P. D., O. V. Sergienko, and D. R. MacAyeal (2010), Transoceanic infragravity
 669 waves impacting Antarctic ice shelves, *Geophysical Research Letters*, *37*(2).
- 670 Bromirski, P. D., A. Diez, P. Gerstoft, R. A. Stephen, T. Bolmer, D. A. Wiens, R. C.
 671 Aster, and A. Nyblade (2015), Ross ice shelf vibrations, *Geophysical Research Letters*,
 672 *42*(18), 7589–7597.
- 673 Brunt, K. M., E. A. Okal, and D. R. MacAyeal (2011), Antarctic ice-shelf calving trig-
 674 gered by the Honshu (Japan) earthquake and tsunami, March 2011, *Journal of Glaciol-*

- 675 *ogy*, 57(205), 785–788.
- 676 Cathles, L., E. A. Okal, and D. R. MacAyeal (2009), Seismic observations of sea swell on
677 the floating Ross Ice Shelf, Antarctica, *Journal of Geophysical Research: Earth Surface*,
678 114(F2).
- 679 DeFranco, S. J., and J. P. Dempsey (1994), Crack propagation and fracture resistance in
680 saline ice, *Journal of Glaciology*, 40(136), 451–462.
- 681 Doake, C., H. Corr, H. Rott, P. Skvarca, and N. Young (1998), Breakup and conditions for
682 stability of the northern Larsen Ice Shelf, Antarctica, *Nature*, 391(6669), 778–780.
- 683 Duddu, R., and H. Waisman (2013), A nonlocal continuum damage mechanics approach to
684 simulation of creep fracture in ice sheets, *Computational Mechanics*, pp. 1–14.
- 685 Duddu, R., J. Bassis, and H. Waisman (2013), A numerical investigation of surface
686 crevasse propagation in glaciers using nonlocal continuum damage mechanics, *Geo-*
687 *physical Research Letters*, 40(12), 3064–3068.
- 688 Dugdale, D. S. (1960), Yielding of steel sheets containing slits, *Journal of the Mechanics*
689 *and Physics of Solids*, 8(2), 100–104.
- 690 Fretwell, P., H. D. Pritchard, D. G. Vaughan, J. Bamber, N. Barrand, R. Bell, C. Bianchi,
691 R. Bingham, D. Blankenship, G. Casassa, et al. (2013), Bedmap2: improved ice bed,
692 surface and thickness datasets for antarctica, *The Cryosphere*.
- 693 Freund, L. (1972a), Crack propagation in an elastic solid subjected to general loading i.
694 constant rate of extension, *Journal of the Mechanics and Physics of Solids*, 20(3), 129–
695 140.
- 696 Freund, L. (1972b), Crack propagation in an elastic solid subjected to general loading ii.
697 non-uniform rate of extension, *Journal of the Mechanics and Physics of Solids*, 20(3),
698 141–152.
- 699 Freund, L. B. (1998), *Dynamic fracture mechanics*, Cambridge university press.
- 700 Fricker, H., N. Young, R. Coleman, J. Bassis, and J.-B. Minster (2005), Multi-year mon-
701 itoring of rift propagation on the Amery Ice Shelf, East Antarctica, *Geophysical Re-*
702 *search Letters*, 32(2).
- 703 Gill, A. E. (2016), *Atmosphere and ocean dynamics*, Elsevier.
- 704 Graff, K. F. (2012), *Wave motion in elastic solids*, Courier Corporation.
- 705 Greene, C. A., D. E. Gwyther, and D. D. Blankenship (2017), Antarctic mapping tools for
706 MATLAB, *Computers and Geosciences*, 104, 151–157.
- 707 Greenhill, A.-G. (1886), Wave motion in hydrodynamics, *American Journal of Mathemat-*
708 *ics*, pp. 62–96.
- 709 Griffith, A. A. (1921), The phenomena of rupture and flow in solids, *Philosophical trans-*
710 *actions of the royal society of london. Series A, containing papers of a mathematical or*
711 *physical character*, 221, 163–198.
- 712 Holdsworth, G. (1969), Flexure of a floating ice tongue, *Journal of Glaciology*, 8(54),
713 385–397.
- 714 Holdsworth, G., and J. Glynn (1978), Iceberg calving from floating glaciers by a vibrating
715 mechanism, *Nature*, 274(5670), 464–466.
- 716 Holland, P. R., H. F. Corr, D. G. Vaughan, A. Jenkins, and P. Skvarca (2009), Marine ice
717 in Larsen ice shelf, *Geophysical Research Letters*, 36(11).
- 718 Hulbe, C. L., C. LeDOUX, and K. Cruikshank (2010), Propagation of long fractures in
719 the Ronne Ice Shelf, antarctica, investigated using a numerical model of fracture propa-
720 gation, *Journal of Glaciology*, 56(197), 459–472.
- 721 Irwin, G. R. (1957), Analysis of stresses and strains near the end of a crack traversing a
722 plate, *Journal of applied mechanics*, 24(3), 361–364.
- 723 Jacobs, S., D. MacAyeal, and J. Ardai (1986), The recent advance of the Ross Ice Shelf
724 Antarctica, *Journal of Glaciology*, 32(112), 464–474.
- 725 Jansen, D., A. Luckman, B. Kulesa, P. R. Holland, and E. C. King (2013), Marine ice
726 formation in a suture zone on the Larsen C Ice Shelf and its influence on ice shelf dy-
727 namics, *Journal of Geophysical Research: Earth Surface*, 118(3), 1628–1640.

- 728 Joughin, I., and D. R. MacAyeal (2005), Calving of large tabular icebergs from ice shelf
729 rift systems, *Geophysical research letters*, 32(2).
- 730 Keys, H. J., S. S. Jacobs, and L. W. Brigham (1998), Continued northward expansion of
731 the Ross Ice Shelf, Antarctica, *Annals of Glaciology*, 27, 93–98.
- 732 Konovalov, Y. (2014), Ice-shelf resonance deflections modelled with a 2-D elastic centre-
733 line model, *Phys. Rev. Res. Int*, 4, 9–29.
- 734 Krawczynski, M. J., M. D. Behn, S. B. Das, and I. Joughin (2009), Constraints on the lake
735 volume required for hydro-fracture through ice sheets, *Geophysical Research Letters*,
736 36(10).
- 737 Krug, J., J. Weiss, O. Gagliardini, and G. Durand (2014), Combining damage and fracture
738 mechanics to model calving, *The Cryosphere Discussions*, 8(1), 1111–1150.
- 739 Larour, E., E. Rignot, and D. Aubry (2004a), Processes involved in the propagation of
740 rifts near Hemmen ice rise, Ronne ice shelf, Antarctica, *Journal of Glaciology*, 50(170),
741 329–341.
- 742 Larour, E., E. Rignot, and D. Aubry (2004b), Modelling of rift propagation on Ronne Ice
743 Shelf, Antarctica, and sensitivity to climate change, *Geophysical research letters*, 31(16).
- 744 LeDoux, C. M., C. L. Hulbe, M. P. Forbes, T. A. Scambos, and K. Alley (2017), Struc-
745 tural provinces of the Ross Ice Shelf, Antarctica, *Annals of Glaciology*, pp. 1–11.
- 746 Lemaitre, J. (1985), A continuous damage mechanics model for ductile fracture, *Transac-
747 tions of the ASME. Journal of Engineering Materials and Technology*, 107(1), 83–89.
- 748 Lipovsky, B. P., and E. M. Dunham (2015), Vibrational modes of hydraulic fractures: In-
749 ference of fracture geometry from resonant frequencies and attenuation, *Journal of Geo-
750 physical Research: Solid Earth*, 120(2), 1080–1107.
- 751 Lipovsky, B. P., and E. M. Dunham (2016), Tremor during ice-stream stick slip, *The
752 Cryosphere*, 10(1), 385–399.
- 753 Lipovsky, B. P., and E. M. Dunham (2017), Slow-slip events on the Whillans Ice Plain,
754 Antarctica, described using rate-and-state friction as an ice stream sliding law, *Journal
755 of Geophysical Research: Earth Surface*, 122(4), 973–1003.
- 756 MacAyeal, D. R., E. Rignot, and C. L. Hulbe (1998), Ice-shelf dynamics near the
757 front of the Filchner-Ronne Ice Shelf, Antarctica, revealed by sar interferometry:
758 model/interferogram comparison, *Journal of Glaciology*, 44(147), 419–428.
- 759 MacAyeal, D. R., E. A. Okal, R. C. Aster, J. N. Bassis, K. M. Brunt, L. M. Cathles,
760 R. Drucker, H. A. Fricker, Y.-J. Kim, S. Martin, et al. (2006), Transoceanic wave prop-
761 agation links iceberg calving margins of Antarctica with storms in tropics and Northern
762 Hemisphere, *Geophysical Research Letters*, 33(17).
- 763 Malvern, L. E. (1969), *Introduction to the Mechanics of a Continuous Medium*, Monograph,
764 Pearson.
- 765 McGrath, D., K. Steffen, H. Rajaram, T. Scambos, W. Abdalati, and E. Rignot (2012),
766 Basal crevasses on the Larsen C Ice Shelf, Antarctica: Implications for meltwater pond-
767 ing and hydrofracture, *Geophysical Research Letters*, 39(16).
- 768 McGrath, D., K. Steffen, P. R. Holland, T. Scambos, H. Rajaram, W. Abdalati, and E. Rig-
769 not (2014), The structure and effect of suture zones in the Larsen C Ice Shelf, Antarc-
770 tica, *Journal of Geophysical Research: Earth Surface*, 119(3), 588–602.
- 771 Munk, W. H., G. Miller, F. Snodgrass, and N. Barber (1963), Directional recording of
772 swell from distant storms, *Philosophical Transactions of the Royal Society of London.
773 A*, 255(1062), 505–584.
- 774 Nemat-Nasser, S., A. Oranratnachai, and L. Keer (1979), Spacing of water-free crevasses,
775 *Journal of Geophysical Research: Solid Earth*, 84(B9), 4611–4620.
- 776 Plate, C., R. Müller, A. Humbert, and D. Gross (2012), Evaluation of the criticality of
777 cracks in ice shelves using finite element simulations, *The Cryosphere*, 6(5), 973.
- 778 Powell, A. (2015), Frozen South: Ice Breakout, <https://vimeo.com/159039693>.
- 779 Pralong, A., and M. Funk (2005), Dynamic damage model of crevasse opening and appli-
780 cation to glacier calving, *Journal of Geophysical Research: Solid Earth*, 110(B1).

- 781 Press, F., and M. Ewing (1951), Propagation of elastic waves in a floating ice sheet, *Eos,*
782 *Transactions American Geophysical Union*, 32(5), 673–678.
- 783 Reeh, N. (1968), On the calving of ice from floating glaciers and ice shelves, *Journal of*
784 *Glaciology*, 7(50), 215–232.
- 785 Rice, J. R. (1968), A path independent integral and the approximate analysis of strain con-
786 centration by notches and cracks, *Journal of applied mechanics*, 35(2), 379–386.
- 787 Rice, J. R. (2001), New perspectives on crack and fault dynamics, in *Mechanics for a New*
788 *Millennium*, pp. 1–24, Springer.
- 789 Rice, J. R., and N. Levy (1972), The part-through surface crack in an elastic plate, *Jour-*
790 *nal of Applied Mechanics*, 39(1), 185–194.
- 791 Rice, J. R., and D. M. Tracey (1969), On the ductile enlargement of voids in triaxial stress
792 fields, *Journal of the Mechanics and Physics of Solids*, 17(3), 201–217.
- 793 Rignot, E., and D. R. MacAyeal (1998), Ice-shelf dynamics near the front of the Filchner
794 Ronne Ice Shelf, Antarctica, revealed by SAR interferometry, *Journal of Glaciology*,
795 44(147), 405–418.
- 796 Rignot, E., G. Casassa, P. Gogineni, W. Krabill, A. Rivera, and R. Thomas (2004), Accel-
797 erated ice discharge from the Antarctic Peninsula following the collapse of Larsen B ice
798 shelf, *Geophysical Research Letters*, 31(18).
- 799 Rist, M., P. Sammonds, H. Oerter, and C. Doake (2002), Fracture of Antarctic shelf ice,
800 *Journal of Geophysical Research: Solid Earth*, 107(B1).
- 801 Robin, G. d. Q. (1979), Formation, flow, and disintegration of ice shelves, *Journal of*
802 *Glaciology*, 24(90), 259–271.
- 803 Scambos, T., T. Haran, M. Fahnestock, T. Painter, and J. Bohlander (2007), MODIS-based
804 mosaic of Antarctica (MOA) data sets: Continent-wide surface morphology and snow
805 grain size, *Remote Sensing of Environment*, 111(2-3), 242–257.
- 806 Scambos, T., H. A. Fricker, C.-C. Liu, J. Bohlander, J. Fastook, A. Sargent, R. Massom,
807 and A.-M. Wu (2009a), Ice shelf disintegration by plate bending and hydro-fracture:
808 Satellite observations and model results of the 2008 Wilkins Ice Shelf break-ups, *Earth*
809 *and Planetary Science Letters*, 280(1), 51–60.
- 810 Scambos, T., J. Bohlander, and B. Raup (2009b), Images of Antarctic ice shelves, *National*
811 *Snow and Ice Data Center*, online available at: <http://nsidc.org/data/iceshelves/images>.
- 812 Scambos, T. A., J. Bohlander, C. u. Shuman, and P. Skvarca (2004), Glacier acceleration
813 and thinning after ice shelf collapse in the Larsen B embayment, Antarctica, *Geophys-*
814 *ical Research Letters*, 31(18).
- 815 Schulson, E. M., P. Duval, et al. (2009), *Creep and fracture of ice*, vol. 1, Cambridge Uni-
816 versity Press Cambridge.
- 817 Sergienko, O. (2010), Elastic response of floating glacier ice to impact of long-period
818 ocean waves, *Journal of Geophysical Research: Earth Surface*, 115(F4).
- 819 Sergienko, O. (2013), Normal modes of a coupled ice-shelf/sub-ice-shelf cavity system,
820 *Journal of Glaciology*, 59(213), 76–80.
- 821 Sergienko, O. (2017), Behavior of flexural gravity waves on ice shelves: Application to the
822 Ross Ice Shelf, *Journal of Geophysical Research: Oceans*.
- 823 Shabtaie, S., and C. R. Bentley (1982), Tabular icebergs: implications from geophysical
824 studies of ice shelves, *Journal of Glaciology*, 28(100), 413–430.
- 825 Sih, G. C. (2012), *Plates and shells with cracks: a collection of stress intensity factor solu-*
826 *tions for cracks in plates and shells*, vol. 3, Springer Science & Business Media.
- 827 Smith, R. (1976), The application of fracture mechanics to the problem of crevasse pen-
828 etration, *Journal of Glaciology*, 17(76), 223–228.
- 829 Van der Veen, C. (1998), Fracture mechanics approach to penetration of surface crevasses
830 on glaciers, *Cold Regions Science and Technology*, 27(1), 31–47.
- 831 Vaughan, D. G. (1995), Tidal flexure at ice shelf margins, *Journal of Geophysical Re-*
832 *search: Solid Earth*, 100(B4), 6213–6224.

- 833 Walker, C., J. Bassis, H. Fricker, and R. Czerwinski (2013), Structural and environmental
834 controls on Antarctic ice shelf rift propagation inferred from satellite monitoring, *Jour-*
835 *nal of Geophysical Research: Earth Surface*, *118*(4), 2354–2364.
- 836 Walker, C. C., J. N. Bassis, H. A. Fricker, and R. J. Czerwinski (2015), Observations of
837 interannual and spatial variability in rift propagation in the Amery Ice Shelf, Antarctica,
838 2002–14, *Journal of Glaciology*, *61*(226), 243–252.
- 839 Wang, R., and H. H. Shen (2010), Gravity waves propagating into an ice-covered ocean:
840 A viscoelastic model, *Journal of Geophysical Research: Oceans*, *115*(C6).
- 841 Weertman, J. (1957), Deformation of floating ice shelves, *Journal of glaciology*, *3*(21), 38–
842 42.
- 843 Weertman, J. (1971), Theory of water-filled crevasses in glaciers applied to vertical
844 magma transport beneath oceanic ridges, *Journal of Geophysical Research*, *76*(5), 1171–
845 1183.
- 846 Weertman, J. (1973), Can a water-filled crevasse reach the bottom surface of a glacier,
847 *IASH publ*, *95*, 139–145.
- 848 Weiss, J. (2004), Subcritical crack propagation as a mechanism of crevasse formation and
849 iceberg calving, *Journal of Glaciology*, *50*(168), 109–115.
- 850 Williams, R., and E. Robinson (1981), Flexural waves in the Ross Ice Shelf, *Journal of*
851 *Geophysical Research: Oceans*, *86*(C7), 6643–6648.
- 852 Yu, H., E. Rignot, M. Morlighem, and H. Seroussi (2017), Iceberg calving of Thwaites
853 Glacier, West Antarctica: full-Stokes modeling combined with linear elastic fracture
854 mechanics, *The Cryosphere*, *11*(3), 1283–1296, doi:10.5194/tc-11-1283-2017.